

Quantifying Pore Width Effects on Diffusivity via a Novel 3D Stochastic Approach with Input from Atomistic Molecular Dynamics Simulations

Maria Apostolopoulou¹, Mirella S. Santos², Muhammad Hamza², Tai Bui¹, Ioannis G. Economou², Michail Stamatakis¹, and Alberto Striolo^{1,}*

¹Department of Chemical Engineering, University College London, Torrington Place, London, WC1E 7JE, United Kingdom

²Chemical Engineering Program, Texas A&M University at Qatar, Post Office Box 23874, Doha, Qatar

Keywords: Kinetic Monte Carlo, Fluid Transport, Permeability, Unconventional Hydrocarbons, Catalysis, Confinement

ABSTRACT

The increased production of unconventional hydrocarbons emphasizes the need of understanding the transport of fluids through narrow pores. Although it is well known that confinement affects fluids structure and transport, it is not yet possible to quantitatively predict properties such as diffusivity as a function of pore width in the range of 1-50 nm. Such pores are commonly found in shale rocks, but also in a wide range of engineering materials, including catalysts. We propose here a novel and computationally efficient methodology to obtain accurate diffusion coefficient predictions as a function of pore width for pores carved out of common materials, such as silica, alumina, magnesium oxide, calcite and muscovite. We implement atomistic molecular dynamics (MD) simulations to quantify fluid structure and transport within 5 nm-wide pores, with particular focus on the diffusion coefficient within different pore regions. We then use these data as input to a bespoke stochastic kinetic Monte Carlo (KMC) model, developed to predict fluid transport in mesopores. The KMC model is used to extrapolate the fluid diffusivity for pores of increasing width. We validate the approach against atomistic MD simulation results obtained for wider pores. When applied to supercritical methane in slit-shaped pores, our methodology yields data within 10% of the atomistic simulation results, with significant savings in computational time. The proposed methodology, which combines the advantages of MD and KMC simulations, is used to generate a digital library for the diffusivity of gases as a function of pore chemistry and pore width and could be relevant for a number of applications, from the prediction of hydrocarbon transport in shale rocks to the optimization of catalysts, when surface-fluid interactions impact transport.

1. INTRODUCTION

The Energy Information Administration (EIA) projects a 28% increase in world energy use between 2015 and 2040.¹ In 2017, according to BP Energy Outlook, the global primary energy consumption grew by 2.2%, on a yearly basis. The production of natural gas increased by 4% between 2017 and 2018, after three years of slowdown.^{1,2} Renewables and natural gas are expected to account for 85% of the growth in primary energy demand by 2040.² This ever-increasing demand for energy is the root for the wide interest in unconventional hydrocarbons. Hydraulic fracturing and the ability to drill extended-reach horizontal wells established the Barnett Shale as the largest gas producing formation in the US in 2008. Stemming from this success, a shale gas revolution occurred in the United States in the early 21st Century.^{3,4}

At present, the development and profitability of a shale play depends on its permeability. Shale rocks consist of organic and inorganic matter with pore sizes ranging from the nano- to the meso-scale.⁵ Advanced imaging of core samples reveals the complexity of the pore system within the shale matrix.^{6,7} The properties that define shale permeability are mainly porosity (pore size distribution – PSD), organic content (% of total organic carbon - TOC), and mineralogy.⁸ The inorganic matter of shales is predominantly made up of quartz, carbonate and clays.^{9–13} State-of-the-art computational methods have been developed to couple imaging data that reveal chemical composition and pore size distribution of a rock sample, to generate realistic pore networks that resemble those in shales, and then perform mesoscale simulations to estimate permeability using, e.g., computational fluid dynamics.^{14–17}

The accuracy of such calculations depends on several factors, most importantly on the quality of input data used to generate the pore networks. When implementing lattice-based approaches, both stochastic and deterministic, the transport properties assigned to the various pores and connections in the pore network must be carefully selected. Due to the significantly small scale of

the pores often found in shale formations, but also in engineering materials such as catalysts, atomistic molecular dynamics and Monte Carlo simulations (MD and MC) have been widely used to quantify fluid transport through narrow pores as well as fluid structure and preferential adsorption.¹⁸ The atomistic simulations allow the user to define 1) the chemical composition of the pores, 2) their shape and size, 3) the fluids and mixtures that fill the pores, and 4) conditions such as temperature and pressure. For example, Sui et al. studied adsorption and transport of methane in dry and water-wet montmorillonite clays and found that the methane self-diffusion coefficient increases rapidly as the pore size increases.¹⁹ Vasileiadis et al. investigated the role of porosity on adsorption and transport of CH₄, C₂H₆, CO₂ and their mixtures, in over-mature type II kerogen under various temperature and pressure conditions.²⁰ Wang et al. investigated the transport of supercritical methane in clay, calcite and organic matter as a function of pore size, pressure, and water content.²¹ Phan et al., calculated the permeability of methane through 1 nm-wide pores filled with water,²² and Bui et al., identified the correspondent transport mechanisms by analyzing the free energy landscape within various pores.²³

Although atomistic simulations can provide an accurate understanding of the transport mechanisms in confinement, upscaling to larger time and length scales requires significant, sometimes prohibitive computational effort. As a result, the systems investigated are frequently composed of a single pore, and a limited number of pore sizes/chemistries are explicitly considered.^{24,25} To bridge the gap from atomistic simulations in single narrow pores to large scale systems, transport models that correlate diffusivity and/or permeability to pore characteristics have been developed. Typically, these models account for three diffusion mechanisms: Fickian, Knudsen, and surface diffusion.^{26–28} The contribution of each mechanism to the overall fluid transport is described by coefficients, derived either from experimental or computational data.

Although many transport models have been proposed, a gas transport model that simultaneously considers organic nanopores, inorganic nanopores and micro-fractures is not yet available. Further, when using the available models at conditions different than those used to construct them, re-parameterization becomes mandatory.^{29,30}

Apostolopoulou et al. recently implemented stochastic kinetic Monte Carlo (KMC) simulations to study fluid transport across pore networks.³¹ KMC methods can access long time scales (up to ms and, in some cases, hours) and large spatial scales (nm to μm) at comparatively low computational expense.^{32,33} For example, in a bottom-up 1D approach, Apostolopoulou et al. 1) used previously-reported MD data to inform the KMC model, 2) simplified a 3D, 2-phase system consisting of confined liquid water and methane into a 1D problem, and 3) obtained KMC transport data in quantitative agreement with atomistic MD simulations at a fraction of the computational cost.³⁴ Apostolopoulou et al. recently extended the analysis to a 2D network,³¹ constructed using imaging data, previously reported, for an Eagle Ford shale sample, as well as PSDs.³⁵ The transport model of Naraghi and Javadpour was used to assign transport properties to the pores within the network.³⁵ Apostolopoulou et al.'s KMC approach was then validated both against deterministic models and experimental data.

In this contribution, we address whether a stochastic approach based on our KMC model could be used to upscale MD simulation results and predict fluid diffusivity in meso-scale pores when results are available for narrow pores. We develop a bespoke model that uses MD data as input to a KMC model framework. We consider slit-shaped pores carved out of five solid supports that resemble minerals typically found in the inorganic matter of shale formations. The fluid considered is supercritical methane. The MD simulations are conducted for pores of width 5 nm. Equilibrium NVT simulations yield density profiles, which we use to differentiate 'adsorbed' and 'bulk'

methane layers within the pores. We then calculate the diffusivity of methane in such areas, confirming that, in the pores center, methane behavior resembles that in the bulk. We use these data to construct and inform our 3D KMC model, which contains 3 distinct regions with substrate-specific transport properties. The stochastic simulations yield the effective diffusivity of methane as a function of pore width. The results are validated by reproducing independent atomistic MD simulations conducted in wider pores. The KMC model is then used to generate a digital library where methane diffusivity is quantified as a function of pore chemistry (within the 5 materials considered here) as well as of pore width (up to ~ 60 nm). Such digital libraries could be used to describe 3D networks consisting of pores with varying chemical compositions and PSDs. This will be the focus of our future work.

The remainder of this article is organized as follows: in Section 2 we describe the methods and algorithms implemented in this work, from the atomistic simulations to the 3D KMC model used to predict diffusivity. In Section 3 we discuss our results, from the details obtained with atomistic resolution for supercritical methane in the model pores, to meso-scale KMC predictions of diffusivity, which yield the digital library, including the validation tests we conducted. Finally, in Section 4 we summarize our findings, with a brief overview of possible applications of our bespoke approach, as well as of some of its limitations.

2. COMPUTATIONAL DETAILS

We conducted a series of equilibrium molecular dynamics (EMD) simulations to obtain the required input data and validate our 3D KMC model using 5 nm and 10 nm slit pores (in one case, a 25 nm pore was also used). We describe here, briefly, the models implemented to simulate the solid substrates and the force fields used to model methane and methane-surface interactions. We

then discuss the setup of the simulated systems and the algorithms utilized, with particular attention to the development and validation of the stochastic KMC model.

2.1 Solid Supports

We considered slit-shaped pores obtained from five model materials: silica, alumina, MgO, calcite, and muscovite, which represent minerals typically found in the inorganic matter of shale formations.^{9–13} Details about the fabrication of the model materials have been reported elsewhere.^{36–43} Characterization of the five solid supports and comparisons, in terms of free energy landscapes and methane solvation free energies, are discussed by Bui et al.²³ Further characterization of hydrated silica, alumina, and MgO pores has also been achieved by calculating potential of mean force profiles.²² In the models implemented here, all the non-bridging oxygen atoms on silica and alumina surfaces were protonated; MgO, muscovite, and calcite surfaces were not hydroxylated. The latter modelling choice is an oversimplification, as discussed by Bui et al.²³ and Phan et al.²², but it allows us to understand, computationally, the effects of fluid-solid interactions on fluid transport under confinement. The substrates have a surface parallel to the X–Y plane of the simulation box. The X and Y dimensions of the substrates are shown in Table 1. Each pore was obtained by separating the solid substrates along the Z direction, which is perpendicular to the X–Y plane. The Z dimension of the simulation box, which includes pore and substrate, is also presented in Table 1 for silica, MgO, alumina, calcite and muscovite pores. These dimensions allowed us to maintain the pore width at 5 nm in all the systems considered. To obtain pores with width 10 nm, the Z dimension was increased (see Table 1). The pore width was defined as the shortest center-to-center distance between surface oxygen atoms across the pore volume. We also considered one pore of width 25 nm made of calcite.

Table 1. Simulation box dimensions used to simulate 5 nm (Z_1) and 10 nm (Z_2) wide pores using five solid supports.

Substrate	Dimensions in nm			
	X	Y	Z_1	Z_2
Silica	5.20	10.10	8.30	13.30
MgO	5.50	10.40	7.50	12.50
Alumina	5.12	9.12	7.41	12.41
Calcite	4.86	9.00	9.90	14.90
Muscovite	4.73	7.35	8.50	13.50

2.2 Force Fields

We used the force fields previously employed by Bui et al.²³ To simulate silica, MgO, alumina, and muscovite, we implemented CLAYFF, while calcite was described using the force field developed by Xiao et al.^{44,45} In the calcite substrate, calcium and carbon atoms were kept rigid, whereas the oxygen atoms were allowed to move freely. In the other materials, silicon, aluminum, and oxygen atoms were held at fixed positions while the surface hydroxyl hydrogen atoms were allowed to vibrate. All atoms in MgO were kept rigid.

We implemented the transferable potentials for phase equilibria in the united atom formalism (TraPPE-UA) to model methane in all solid substrates, except calcite.⁴⁶ In the latter substrate, to be consistent with Bui et al., we used the OPLS-UA forcefield to model methane.⁴⁷ Both TraPPE-UA and OPLS-UA forcefields yield values for the self-diffusion coefficient of methane that are in relatively good agreement with experiments. According to Ho et al., the % deviation between MD simulations at 300 K using the TraPPE-UA and experiments at 297 K is 1%-6% for pressures

between 50 and 300 atm.⁴⁸ Feng et al., reported deviations between the diffusion coefficient of methane calculated using the OPLS-AA forcefield and experiments in the range 1-4% when the temperature is 295 K and the pressure ranges between 11 and 207 MPa.⁴⁹

In the present simulations, nonbonded interactions were modeled by means of dispersive and electrostatic forces. The electrostatic interactions were described by the Coulombic potential, with long-range corrections treated using the particle mesh Ewald (PME) method.⁵⁰ Dispersive interactions were modeled by 12–6 Lennard-Jones (LJ) potentials. The LJ parameters for unlike interactions were determined by Lorentz–Berthelot combining rules from the values of like components.^{51,52} The cut-off distance for all interactions was set to 1.4 nm. We did not apply long-range corrections; according to Siperstein et al., consistency in the cut-off radius is more important than the inclusion of long-range corrections to the energy.⁵³

2.3 MD Simulation Setup and Algorithms

The simulation setup for the pores considered in this study mimics the one adapted by Bui et al.,²³ which was implemented to investigate methane transport through hydrated 1 nm-wide nanopores. To directly compare results among the five substrates, we kept the overall fluid density at $0.01314 \text{ atoms}/\text{\AA}^3 \sim 0.350 \text{ g}/\text{cm}^3$ in all pores. To prepare systems with the desired density, we simulated the slit pores surrounded by a bulk reservoir within a periodic simulation box. We monitored the pressure at the bulk reservoir regions using the density profiles and the Peng-Robinson equation of state, while simulating different amounts of methane, under the assumption that the methane in the bulk region behaves like a macroscopic fluid. The methane molecules were initially added to the reservoir. The temperature was kept at 300 K for all substrates. As the simulations progressed, some fluid molecules entered the pore. Once the reservoir pressure for all substrates was constant at 87 MPa, we counted the molecules that had entered the five pores. We

then removed the reservoir and inserted the desired amounts of methane to the 5 pores, which, because of periodic boundary conditions, were now effectively infinite along X and Y dimensions. It was necessary to introduce 3450, 3758, 3068, 2874, and 2284 methane molecules in the 5 nm-wide silica, MgO, alumina, calcite, and muscovite pores, respectively. For the 10 nm pores, we used exactly double the number of molecules just listed. For all solid substrates, the simulation box is periodic in the three directions. A representative simulation snapshot is shown in Figure 1.

An alternative simulation method for determining the amount of gas adsorbed in the slit pores for given temperature and pressure, is grand canonical Monte Carlo.^{54,55} We preferred here the 2-reservoir method coupled with solving the Peng-Robinson equation of state due to simplicity and computational efficiency. We focus here on one set of temperature and pressure, although it should be noted that realistic reservoir conditions show a range of pressures and temperatures. The effect of temperature and pressure on supercritical methane transport through slit-shaped pores has been recently reported by Wang et al.²¹ for various minerals.

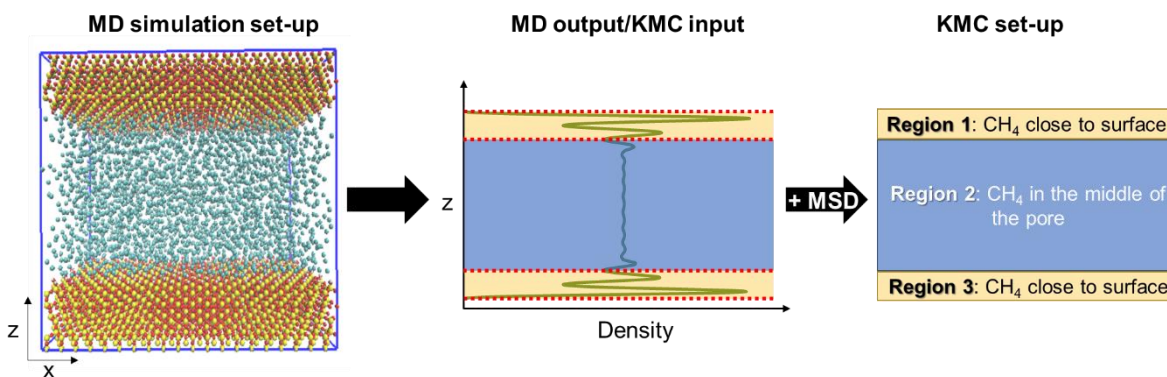


Figure 1. Schematic of the MD simulation set up (left), the criteria for determining the 3 regions that describe the density of confined methane (middle), and a 2D slice of a typical 3D KMC simulation set up (right). In the left panel, for visualization purposes, the solid support is silica. The dashed red lines in the middle panel identify Regions 1, 2, and 3, and serve as guides to the eye.

We performed EMD simulations in the canonical ensemble (NVT) by maintaining constant number of particles (N), simulation volume (V) and temperature (T), using the package

GROMACS, version 5.1.1.^{56,57} The temperature was kept constant at 300 K using 3 Nose-Hoover thermostats, to better control the gas temperature and avoid un-physical phenomena. In the thermostats, the relaxation time was set at 100 fs.^{58,59} Two thermostats were used to control the temperature of the top and bottom solid surfaces, and one to keep the temperature of the methane constant. The leapfrog algorithm was used to solve the equations of motion with 1 fs time step.⁶⁰ To equilibrate the systems, we performed one NVT simulation for 50 ns for each pore. To confirm equilibrium was reached, we tested the convergence of methane's density profile along the Z direction. We then performed 3 ns production runs at 300 K for each system to collect data. Following the same protocol, we also performed 3 independent bulk methane simulations using 1638 CH₄ molecules and a cubic simulation box of size 5 × 5 × 5 nm³.

Once the MD simulations were completed, analysis of the density profiles for methane in the direction perpendicular to the pore surface allowed us to identify 3 regions within each of the pores: Region 1 (R1) and Region 3 (R3) are close to the solid surface; Region 2 (R2) corresponds to the middle of the pore (see Figure 1). As shown in Figure 1, Region 1 and Region 3 were designed to include the first two adsorbed layers, in which it is expected, based on atomistic MD simulation results reported in the literature, that the fluid behavior differs from bulk properties. The thickness of Region 1 and 3 as identified on the various supports is provided in Table 2.

The data obtained from the 5 nm pores, were used as input for our KMC model to predict the diffusion of methane in slit pores of varying width, as detailed in Section 2.4.

We tested the validity of the KMC predictions against MD data obtained for methane within 10 nm - wide pores. In the case of calcite, as discussed in Section 3.1, we found the diffusion to be anisotropic and the solid surface to strongly interact with the methane molecules. To test whether this effect was accurately captured using the KMC model, we also simulated a 25 nm-wide pore

using EMD simulations and performed an additional comparison between EMD and KMC results. Due to the high computational effort required for these simulations, we did not consider any other 25 nm-wide pores in this work. The procedures implemented to simulate 10 and 25 nm-wide pores are similar to those just described for the 5 nm pores.

To analyze the molecular trajectories obtained from EMD simulations, we calculated density, diffusion coefficients, and radial distribution functions (RDFs). For the density analysis, we used bins of width 0.02 nm and we counted the number of molecules as a function of Z. From the density plots, we identified Regions 1, 2, and 3 (see Figure 1 for a schematic of the three regions within the pore). We used the trajectories within each region to calculate the diffusion coefficients for methane in all substrates. We calculated the diffusivity in the X (D_x), Y (D_y), Z (D_z) directions, within the XY plane (D_{xy}), and also the overall (total) diffusivity (D_{xyz}), using Einstein's relation, on the basis of the calculated mean square displacements (MSDs):

$$D_x = \frac{1}{2} \lim_{t \rightarrow \infty} \frac{\langle |x_i(t) - x_i(0)|^2 \rangle}{t} \quad (1)$$

$$D_y = \frac{1}{2} \lim_{t \rightarrow \infty} \frac{\langle |y_i(t) - y_i(0)|^2 \rangle}{t} \quad (2)$$

$$D_z = \frac{1}{2} \lim_{t \rightarrow \infty} \frac{\langle |z_i(t) - z_i(0)|^2 \rangle}{t} \quad (3)$$

$$D_{xy} = \frac{1}{4} \lim_{t \rightarrow \infty} \frac{\langle |\mathbf{r}^{\text{plane}}_i(t) - \mathbf{r}^{\text{plane}}_i(0)|^2 \rangle}{t} \quad (4)$$

$$D_{xyz} = \frac{1}{6} \lim_{t \rightarrow \infty} \frac{\langle |\mathbf{r}_i(t) - \mathbf{r}_i(0)|^2 \rangle}{t} \quad (5)$$

In Eqs. (4-5), $\langle |\mathbf{r}^{\text{plane}}_i(t) - \mathbf{r}^{\text{plane}}_i(0)|^2 \rangle$ and $\langle |\mathbf{r}_i(t) - \mathbf{r}_i(0)|^2 \rangle$ are the MSDs in the XY-plane and XYZ space, respectively, and $\mathbf{r}^{\text{plane}}_i(t) = (x_i(t), y_i(t))$, and $\mathbf{r}_i(t) = (x_i(t), y_i(t), z_i(t))$, respectively. Simonnin et al.,⁶¹ Yeh and Hummer⁶², and Le et al.,⁶³ reported that the diffusion coefficients computed using molecular simulations for fluids confined in wide nanopores suffer from finite-size effects and proposed a correction to overcome these effects. Similarly, Moulton et al., found the use of “large” systems of several thousand molecules is not always adequate for eliminating the dependence of self-diffusion coefficients on system size, and that explicit corrections, such as the Yeh and Hummer correction, must be applied to account for systematic errors.⁶⁴ Based on the latter work, Jamali et al. further proposed a Maxwell–Stefan Yeh and Hummer correction for finite-size effects of computed Maxwell–Stefan diffusion coefficients.⁶⁵ In this study, to correct for possible finite-size artefacts and time-dependent fluctuations, we calculated the diffusion coefficients via the analysis of the correlation functions. The timescale for the diffusion coefficient calculations was 20 ps of simulation run time (which corresponds to 100 “frames” in the simulation). After these 20 ps, $\mathbf{r}_i(0)$ was updated for all molecules. The process was repeated 150 times and the average diffusion coefficient was obtained.

To ensure that methane is at supercritical conditions, we calculated the RDFs at the end of each production run using GROMACS. These data are reported as Supplementary Material.

2.4 3D Kinetic Monte Carlo validation

Our KMC approach, applied to 1D and 2D pore networks, is described by Apostolopoulou et al.^{31,34} The underlying model of the KMC simulation is the Master Equation (Eq. 6), which can be

thought of as a “probability balance”.³³ The Master Equation expresses the rate of change for the probability $P_p(t)$ of finding the system in state p at time t , in terms of the probability influx from other states q , and the probability efflux toward these other states:⁶⁶

$$\frac{dP_p(t)}{dt} = \sum_{q \neq p} W_{pq} P_q(t) - \sum_{q \neq p} W_{qp} P_p(t) \quad (6)$$

The state vectors p and q in Eq. (6) capture the information necessary to describe the location of diffusing fluid particles in the porous network of interest. A state vector stores the number of particles contained in each and every voxel of the network and updates it over time. W_{pq} and W_{qp} are the propensities of the p -to- q and q -to- p transitions, respectively, and are calculated by multiplying the KMC rate constants for these transitions by the number of molecules contained in a voxel. The generic Master Eq. (6) can be used to describe the diffusion of a particle from voxel i,j to voxel $i,j+1$ as follows: in state q , voxel i,j has $n_{i,j} + 1$ particles and voxel $i,j+1$ has $n_{i,j+1} - 1$ particles. The probability per unit time (propensity) for the aforementioned diffusion event to happen is given by the KMC rate for the i,j to $i,j+1$ transition multiplied by the number of molecules in the i,j voxel, $n_{i,j} + 1$. If the transition is performed, the population in the i,j voxel will be $n_{i,j}$, while the number of particles in the $i,j+1$ will be $n_{i,j+1}$, leading to state q .

To develop a 3D KMC model, we extended our 2D model by increasing the number of possible moves a molecule can make from a voxel from 4 to 6 (left, right, up, down, back, and forth). The computational efficiency of the KMC algorithm is strongly dependent on the matrix mesh, as the computational cost to select each KMC step scales with the number of possible events. Considering M to be the number of voxels, for an $M \times M \times M$ system, there are $6 \times M \times M \times M$ possible events at each step. The algorithmic steps implemented for our KMC approach can be found in our recent work.^{31,34} The Mersenne Twister MT19937 uniform random number generator was used to obtain

sequences of random numbers needed for the selection of the event at each step and the calculation of the time required for the transition to happen.⁶⁷

We validated our 3D KMC algorithm using analytical and deterministic methods for a variety of systems. We first tested the model against the analytical solution of the diffusion equation, see Eq. (7), for a homogeneous system with non-periodic boundaries. Then, we considered homogeneous systems with periodic boundaries. At last, we compared the KMC predictions against MD data for three systems with increasing heterogeneity and mixed boundaries.

$$\frac{1}{D} \frac{\partial C}{\partial t} = \frac{\partial^2 C}{\partial x^2} + \frac{\partial^2 C}{\partial y^2} + \frac{\partial^2 C}{\partial z^2} \quad (7)$$

To compare the 3D KMC against the analytical solution of the diffusion equation, we considered a 3 x 3 x 10 lattice. The unit cell size was 1 nm and all boundaries were reflective. We uniformly distributed 1350 molecules in a 3 x 3 x 3 cube from origin O (0,0,0), as shown in Section 3.3, while the rest of the lattice remained empty. The diffusion coefficient in all voxels was set at 1 x 10⁻⁸ m²/s. We allowed the molecules to diffuse and monitored the population in Voxel 5 (5,1,1) and Voxel 10 (10,1,1) as a function of simulation time. A sample was taken every 0.01 ns and the total simulation time was 10 ns. We performed 10 independent simulations and obtained the average population over time in the 2 voxels of interest. The equation of diffusion for a 3D system is shown in Eq. (7), where 0 ≤ x ≤ l_x, 0 ≤ y ≤ l_y, and 0 ≤ z ≤ l_z, D is the diffusion coefficient, and C(x,y,z) is the overall concentration of molecules. For certain types of initial and boundary conditions, the analytical solution of Eq. (7) is the product of the analytical solutions of the three one-spatial-variable problems (C_x(x,t), C_y(y,t), and C_z(z,t)), and hence Eq. (7) can be transformed into Eq.(8):⁶⁸

$$C(t) = C_x(x,t) * C_y(y,t) * C_z(z,t) \quad (8)$$

For reflective periodic boundary systems, where the molecules are initially distributed in a well-defined region $-h_x \leq x \leq h_x$, $-h_y \leq y \leq h_y$, and $-h_z \leq z \leq h_z$ with concentration C_{0x} , C_{0y} , and C_{0z} , initially distributed in the X, Y, and Z dimension, respectively, the concentration distribution over time is described by:⁶⁸

$$C_x(x, t) = \frac{1}{2} C_{0x} * \sum_{n=-\infty}^{n=+\infty} \left\{ \operatorname{erf} \left(\frac{h_x + 2nl_x - x}{2\sqrt{D_x t}} \right) + \operatorname{erf} \left(\frac{h_x - 2nl_x + x}{2\sqrt{D_x t}} \right) \right\} \quad (9)$$

$$C_y(y, t) = \frac{1}{2} C_{0y} * \sum_{n=-\infty}^{n=+\infty} \left\{ \operatorname{erf} \left(\frac{h_y + 2nl_y - y}{2\sqrt{D_y t}} \right) + \operatorname{erf} \left(\frac{h_y - 2nl_y + y}{2\sqrt{D_y t}} \right) \right\} \quad (10)$$

$$C_z(z, t) = \frac{1}{2} C_{0z} * \sum_{n=-\infty}^{n=+\infty} \left\{ \operatorname{erf} \left(\frac{h_z + 2nl_z - z}{2\sqrt{D_z t}} \right) + \operatorname{erf} \left(\frac{h_z - 2nl_z + z}{2\sqrt{D_z t}} \right) \right\} \quad (11)$$

To validate the accuracy of our 3D KMC model, we obtained the analytical solution of the diffusion equation (Eq.7), which is the product of Eqs.(8-11), and compared stochastic vs. analytical results. We found the stochastic approach to be in excellent agreement with the analytical solution of the diffusion equation (see results section).

To test the 3D KMC model for systems with periodic boundary conditions, we used a 5 x 6 x 3 lattice with unit cell size of 1 nm. The lattice was periodic in all directions and the diffusion coefficient was uniform along X, Y, and Z directions, with values ranging from 1.3 to 2.3 x 10⁻⁸ m²/s (target diffusivity). A single molecule was inserted in a random position and was allowed to diffuse. Its trajectory was monitored for 70 ns, with samples extracted every 0.7 ns. For every value of the diffusion coefficient selected (target), we performed 3 independent runs. From the stochastic trajectories obtained, we calculated the diffusion coefficient of the particle and compared the diffusivity calculated against the input diffusion coefficient (target). The results

showed perfect agreement between input and output diffusion coefficient, further validating our 3D KMC model.

We previously discussed the appeal of a 2D KMC model to quantify the effect of heterogeneity within a pore network in terms of medium effective permeability.³¹ We test here the accuracy of our bespoke 3D KMC model, while considering systems with strong fluid-surface interactions and increasing degree of heterogeneity. We used the 5 nm silica set up and increased the ϵ (epsilon) parameter that describes methane-silicon and methane-hydroxyl interactions 5 and 25 times. The resulting force field is not realistic, but it provides an artificial system with strong surface-fluid attractions. We used 3000 methane molecules to fill each artificial system and compared the results obtained from all three cases. For comparison, we used diffusion coefficient values predicted from the EMD simulations within the three regions (R1, R2, and R3) using a set-up similar to the one presented in Figure 1. We calculated the overall diffusion coefficient of methane using EMD simulations and our 3D KMC model. At the end, we compared the coefficients obtained from the two methods and found the results to be in excellent agreement. For each system, we performed 3 independent EMD runs and calculated the mean error using the standard error equation:

$$\overline{\text{Error}} = \frac{\text{STD}(D(i))}{\sqrt{n}} \quad (12)$$

In Eq. (12), STD is the standard deviation, $D(i)$ is the diffusion coefficient for each independent run, and n is the number of independent runs. For these calculations, $i=[1,3]$ and hence $n=3$.

2.5 3D Kinetic Monte Carlo Setup

The bespoke 3D KMC model was set up to mimic the EMD slit pore described in Figure 1. The simulation boxes were periodic along X and Y directions and reflective on Z, to represent the pore

surface. To set up the transition rates, r^{KMC} , required to describe the probability of methane moving from one voxel to another within the simulation box, we considered kinetic barriers consistent with the diffusion coefficients in Regions 1, 2 and 3, using Eq. 13:^{69,70}

$$r^{\text{KMC}} = \frac{D}{l^2} \quad (13)$$

where D is the diffusion coefficient, and l is the voxel size. We did not consider thermodynamic barriers, as there are no pore-entrance or pore-exit effects in the present model. The diffusion coefficient values from the EMD simulations, for the 5 nm wide pores, were used as input for the stochastic KMC model's Region 1 and 3 (see Figure 1 for a schematic). These values are reported in Section 3.1 for each solid support considered. The diffusion coefficient assigned to Region 2 in our stochastic model, was obtained from bulk EMD simulations: $1.91 \pm 0.08 \times 10^{-8} \text{ m}^2/\text{s}$. We calculated error bars for all the input values used to feed our KMC model, by performing 3 independent EMD simulations for each system. To increase the accuracy and minimize the uncertainty of our stochastic model, we incorporated the error bars calculated when assigning the transition rates for our stochastic approach.

To predict the overall (total) methane diffusivity in large pores, we added the necessary voxels to Region 2. We considered 35 different pore widths for all five substrates. For each pore width, a single molecule was initially placed at a random position. The molecule was allowed to move freely through the simulation box for a total of 70 ns. A sample monitoring the position of the molecule was taken every 0.7 ns. This process was repeated 10 times, while starting the molecule from the same position. At the end of the 10th iteration, a different random position was selected for the molecule and 10 independent runs followed. We considered 75 initial configurations for each pore width simulated. The simulation protocol for the KMC simulations is presented in Figure 2. We monitored the confidence intervals obtained of the diffusion coefficient calculated while

considering different pore sizes for each substrate. Because no overlap was observed, it is concluded that this number of iterations and initializations allowed us to obtain sufficient statistics for the calculation of the molecule's diffusivity.

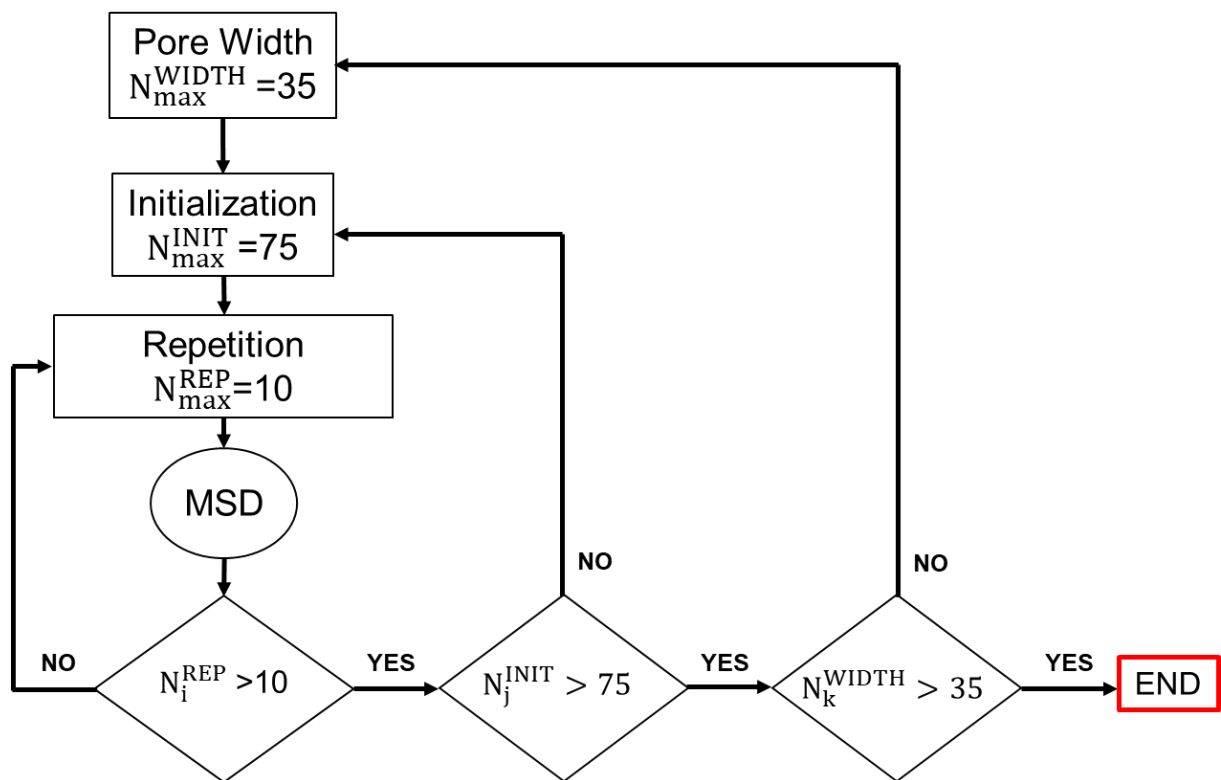


Figure 2. Schematic of the KMC algorithmic steps performed to simulate methane diffusion through pores of varying widths.

3. RESULTS AND DISCUSSION

3.1 Data Analysis

Density plots were obtained for methane inside the 5 nm and 10 nm-wide pores from EMD simulations. Using MATLAB, the density profiles were integrated, and the total amount of molecules was counted in all systems, to ensure less than 1% deviation between the number of molecules in Regions 1 and 3 for both 5 nm and 10 nm-wide pores, and to confirm that equilibrium was reached. From the density profiles, we identified the 3 regions inside the pore (see Table 2)

and counted the number of molecules in each. From the analysis of the density profiles, we confirmed that the regions close to the pore surface (R1 and R3) do not change in thickness when the pore width increases. We also ensured that the difference between the number of molecules in Regions 1 and 3 was less than 5% for each pore-fluid system. We found that the number of molecules adsorbed on the pore surface remains approximately the same (within 5%) when the pore width is increased from 5 to 10 nm. The numbers of molecules found within each of the 3 regions within each substrate are reported in Table 2.

To characterize the structure of the adsorbed methane on each pore surface, we plotted the surface density for methane on the 5 systems, as shown in Figure 3. Methane molecules in the first and second adsorbed layer were considered for this analysis. In some of the substrates, methane shows evidence of patterning (silica, calcite, and muscovite), while in others the molecular distribution is rather uniform.

In Figure 4, we show the density profiles obtained along the Z direction within the 5 nm (black line) and the 10 nm pores (blue line). From the analysis of the density profiles, it is confirmed that the density measured in the middle of all pores remains constant when the pore substrate is changed, and also when the pore width is increased.

Both Figure 4 and Table 2 present the distribution of molecules in Regions 1 and 3. Figure 4 presents the number of molecules within the xy plane as a function of z, while Table 2 reports the total number of molecules counted in x, y, and z directions. In Figure 4, for some of the substrates, the densities for the smaller pores appear as scaled versions of the wider ones. This is because the area below the density is the number of molecules, an intensive variable, which is lower for the smaller pores. However, we note that the number of molecules below the density graphs presented in Figure 4 and reflected in Table 5 for Region 1 and Region 3, as obtained from the 5 nm and 10

nm pores, does not differ. The differences observed in the first peak of the density profiles, for some of the substrates, is possibly related to the proximity of the solid slabs when the pore width is 5 nm. Our diffusion data (see Figure 5) also suggest a small effect due to the proximity of the two pore surfaces when the pore width is 5 nm, compared to data obtained for the 10 nm pores. Hence, it is possible that although the total number of molecules in Regions 1 and 3 is similar in 5 nm and 10 nm pores, this interference of the parallel slabs causes a slightly different spatial arrangement of interfacial molecules, which is captured by the density profiles presented in Figure 4. However, for the purpose of this study, these spatial variations are expected to have an insignificant impact on the diffusion coefficients predicted for wider pores.

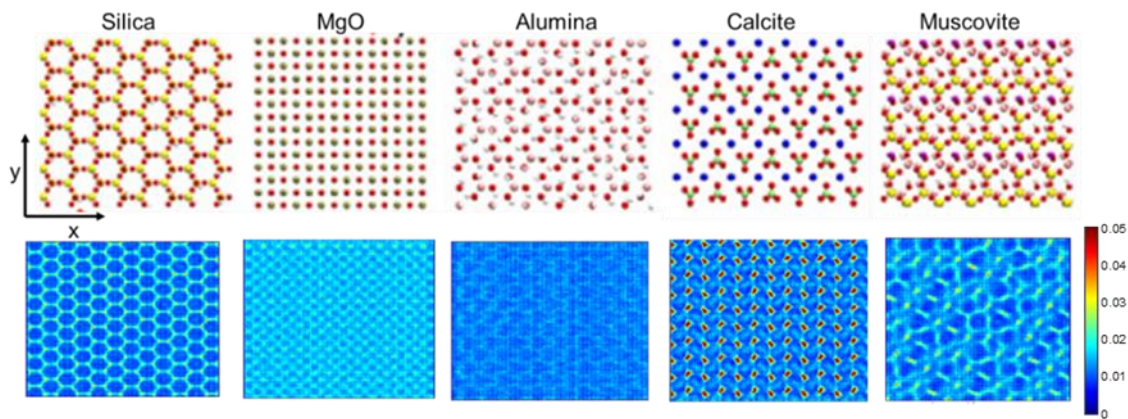


Figure 3. Planar density profile for CH₄ near the surface of the 5 substrates (bottom panel) in atoms/Å³. The top panel shows the composition of the 5 solid supports, as reported by Bui et al.²³ Color code: Si=yellow, Mg= tan, Al=pink, K=purple, C=green, Ca=blue, O=red, and H=white.

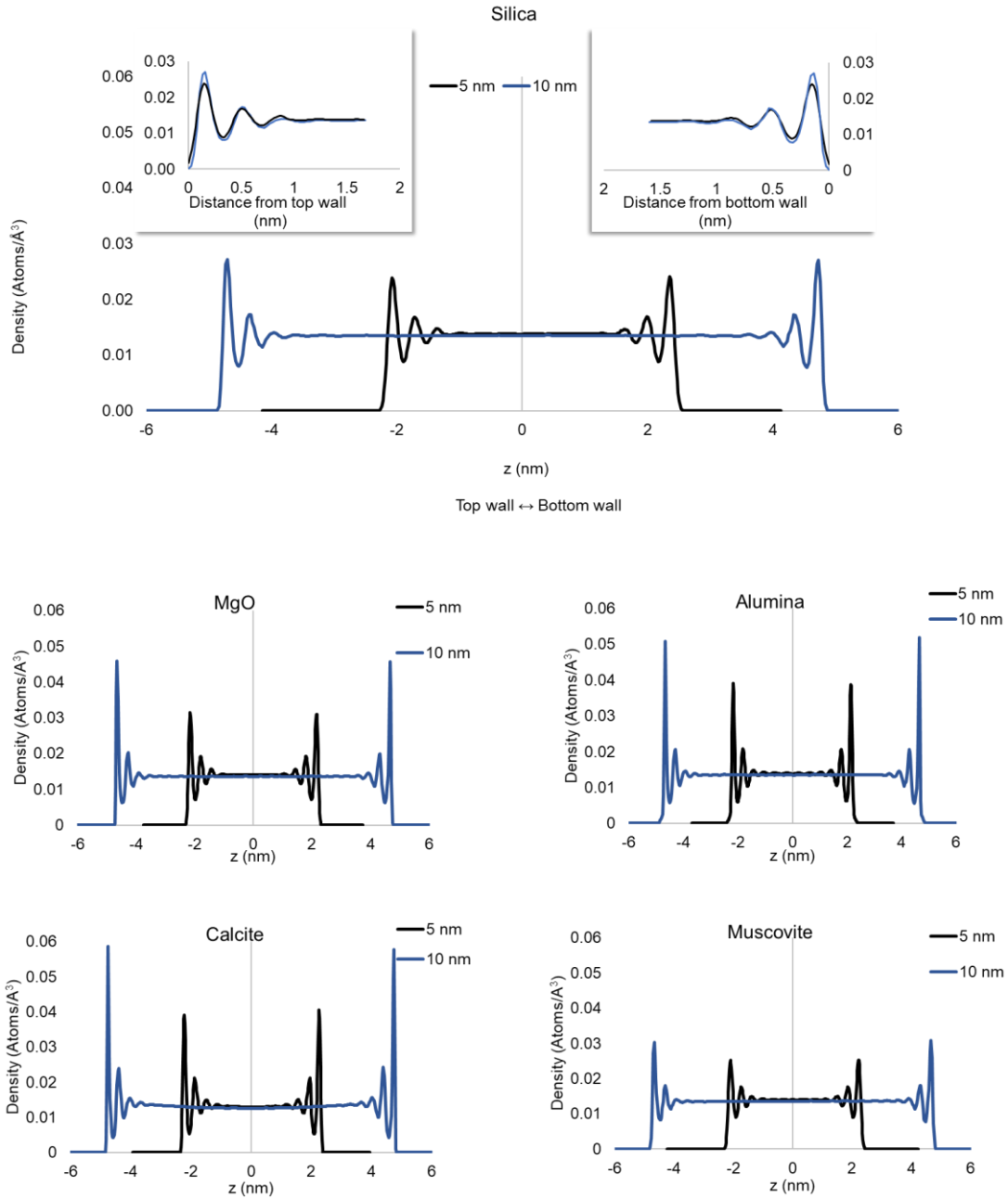


Figure 4. Density profiles for the 5 nm pores (black lines) and the 10 nm pores (blue lines). In the top panel (Silica) we provide the comparison between the 5 nm and 10 nm density profiles as a function of the distance from the pore wall.

Table 2. Comparison between the thicknesses of Regions 1 and 3, the density, and the number of molecules contained in the three regions within slit-shaped pores of width 5 (Z_1) and 10 nm (Z_2).

Substrate	Length (nm)		Density (atoms/nm ³) Molecules			
	R1 & R3 ^{α,β}		R1 & R3 ^{α,β}		R2	
	Z_1	Z_2	Z_1	Z_2	Z_1	Z_2
Silica	0.70	0.70	13.8 506	13.7 505	12.9 2438	13.0 5890
MgO	0.64	0.64	14.8 543	14.2 520	12.6 2672	13.0 6476
Alumina	0.82	0.83	12.2 467	12.0 466	13.6 2134	13.4 5204
Calcite	0.63	0.62	16.4 451	16.8 456	12.1 1972	12.6 4836
Muscovite	0.74	0.72	15.0 385	14.9 372	12.4 1514	12.8 3824
^{α} The values reported for R1 & R3 represent the average of the two regions. ^{β} The % difference between R1 and R3 is less than 5%, confirming the hypothesis regarding the non-changing properties in Regions 1 and 3.						

Within each region, we calculated self-diffusion coefficients (see Computational Details). Figure 5 summarizes the results within 5 (panel A) and 10 nm pores (panel B). The error bars shown in panel (A) are obtained by calculating the standard error, see Eq. (12), from results obtained in 3 independent EMD simulations. Error bars for panel (B) are not available using the standard error formula, since the simulations were performed only once to validate the 3D KMC model and not to be used as inputs. The diffusion coefficient close to the pore surface is lower than in the pore center, where methane exhibits bulk-like behavior. When considering the average values for the 5 nm - wide silica, MgO, alumina, and muscovite pores, the diffusion coefficient in Region 2 is slightly lower than the bulk diffusion coefficient, which was calculated to be $1.91 \pm 0.08 \times 10^{-8}$ m²/s for CH₄ density of 0.01314 atoms/Å³ at 300 K. This is due to the slightly higher density

observed in the middle of these pores. In calcite, the opposite behavior was observed. This is due to the significantly stronger interaction between the fluid and the calcite surface, which yields a higher number of molecules absorbed close to the pore surface, leaving the middle of the pore (Region 2) less crowded, as shown in Table 2. Since fewer molecules are in Region 2, compared to the other substrates, a higher diffusivity was observed in this region. Considering the error bars estimated for diffusivity data, it is observed that all diffusion coefficient values for Region 2, besides calcite's, is consistent with each other. This confirms that the molecules found in Region 2 are beyond the range of surface interactions, when the pores are at least 5 nm wide. Wang et al. reached a similar conclusion, for simulations conducted within 5.4 nm-wide slit-pores made of montmorillonite and calcite and filled with supercritical methane at various densities lower than those considered here.²¹

The diffusion coefficient in Regions 1 and 3 for each substrate is similar, as expected. Moreover, the diffusion coefficient in the regions close to the pore remains almost constant when comparing 5 and 10 nm pores. This is expected, since the number of adsorbed molecules and the thickness of the adsorbed regions remains unaltered while increasing the size of the pore. Wang et al. also observed the mass density of the two adsorbed layers to remain unchanged when simulating supercritical methane confined in 1.8 and 5.4 nm wide calcite pores.²¹ When considering pores of the same material, our results show that the overall (total) diffusivity increases as the pore width increases. We will discuss later at which pore width the diffusivity of confined methane reaches values comparable to those found in the bulk. Our hypothesis is that this increase in diffusivity with pore width is due to the relative increase of the Region 2 thickness when pore width increases. In fact, within Region 2 the diffusion coefficients are significantly higher compared to the areas close to the pore walls.

When considering the diffusivity across the whole pore (Regions 1, 2, and 3), D_x and D_y values calculated for silica, MgO, alumina, and muscovite pores are very similar – less than 1% different, which is an indicator of isotropic diffusion. The same behavior is also observed when comparing the D_x and D_y values in Regions 1, 2, and 3 individually (see Figure 6). However, within calcite pores, the D_x and D_y values in Regions 1 and 3 are significantly different, approximately 33%, 40%, and 17%, when considering 5, 10, and 25 nm pores, respectively, as presented in Figure 7. In the middle of the pore, Region 2, the % difference between the D_x and D_y values is significantly smaller, as the effect of the surface has vanished. Similar anisotropic effects, in the region close to the calcite surface, were also reported by Bui et al.²³ and Franco et al.⁷¹ Bui et al., explained the anisotropic behavior of methane in hydrated calcite nanopores using free energy landscape calculations to further characterize the pore surfaces, as in that case the pores were filled with water. They showed that, because of the structure of confined water, the path of minimum resistance for methane diffusion along the Y direction is a straight line, while that along the X direction is zigzag-like.²³ Note that X and Y directions is arbitrary; in the present comparison, we take X and Y directions to be those shown in Figure 3. Franco et al. also observed methane diffusivity along the Y direction to be higher than that along X near the calcite surface for three pore widths.⁷¹ Our results agree with this observation, as shown in Figure 7.

To verify that the thermodynamic conditions inside all pores correspond to supercritical methane, we plotted radial distribution function profiles for methane within the 5 nm pores. Based on the results obtained (reported in Supplementary Material), it was confirmed that methane in Region 2 is at supercritical conditions within all systems considered.

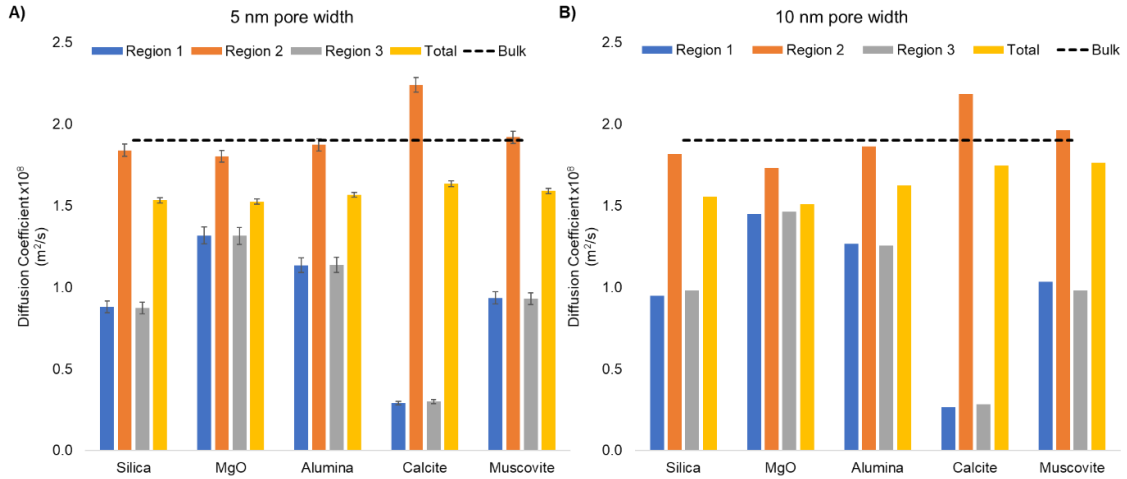


Figure 5. Diffusion coefficients calculated in Regions 1, 2, and 3, as well as in the whole pore (Total), within the pores considered in this study. Panel (A) shows the results obtained for the 5 nm pores, and panel (B) shows those for the 10 nm pores.

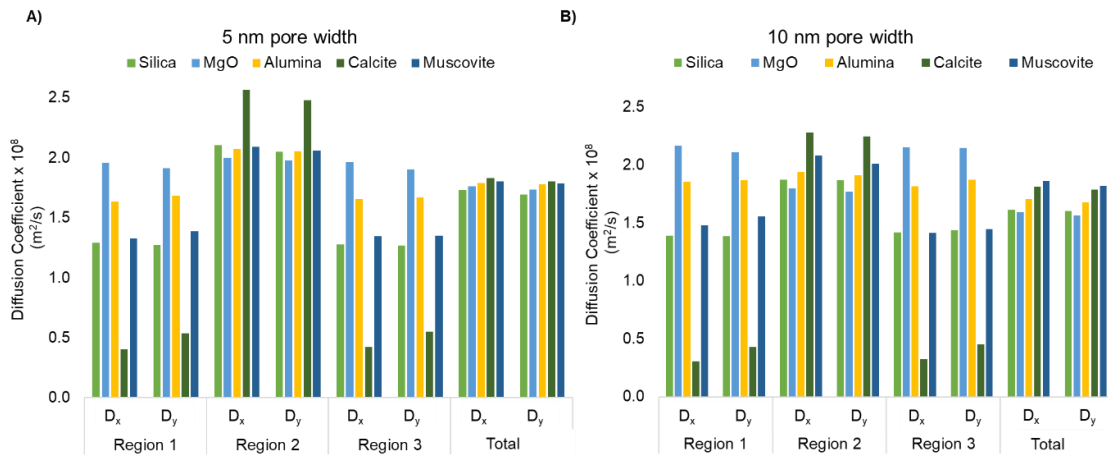


Figure 6. Diffusion coefficients in the X and Y direction, calculated in Regions 1, 2, and 3, as well as in the whole pore (Total). Panel (A) shows the results obtained for the 5 nm pores, and panel (B) shows those for the 10 nm pores.

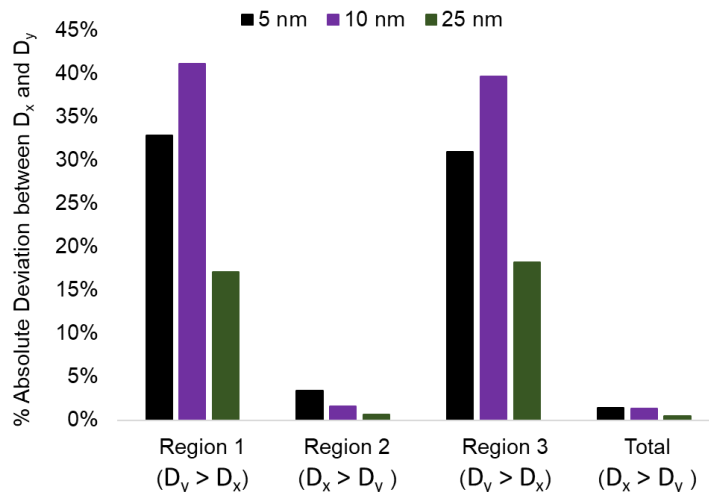


Figure 7. Analysis of anisotropic diffusion in calcite. The y axis shows the % absolute deviation between D_x and D_y values measured in the three regions and the whole (Total) pore, using 3 different pore widths.

3.2 Model systems with exceptionally strong surface-fluid interactions

We performed the analysis discussed above for silica substrates when the force fields were modified to represent exceptionally strong surface-fluid interactions. In these model systems, the methane-silicon and methane-hydroxyl interactions were increased by 5 and 25 times, as described in Section 2.4. In Figures 8 and 9, we compare the results obtained against those gathered within the realistic silica substrate. Note that the number of molecules inserted in the pores was 3000. In Figure 8, we show how the three systems compare in terms of density profiles (panel A) and RDFs (panel B). The diffusion coefficients calculated in the three regions are reported in Figure 9 (panel C, panel D).

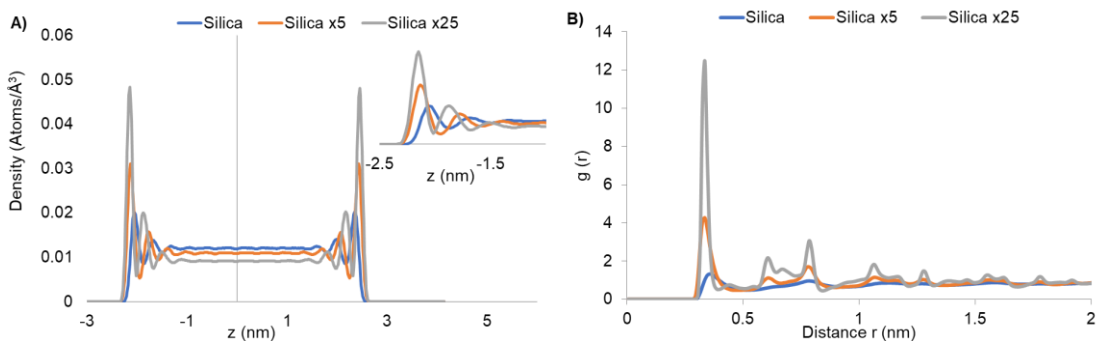


Figure 8. Density (panel a) and RDFs (panel b) for methane within realistic silica pores, as well as within pores with exceptionally strong solid-fluid interactions.

The effect of the strong surface interaction is evident from the density profiles and RDF plots, shown in Figure 8. To further characterize the systems, in Figure 10 we show the planar density profiles parallel to the pore surface for methane within the second adsorption layer, which is determined from the density profiles in Figure 8. According to panel (A), methane molecules preferably arrange in circles surrounding the oxygen atoms on the surface. As the interaction between surface and methane increases (panels B and C), the amount of methane molecules occupying positions aligned with the oxygen atoms increases. This is probably because the maximum number of molecules that can occupy the peripheral positions surrounding the oxygen atoms has been reached, and additional molecules have to occupy positions that correspond to higher conformational energy.

In Figure 9, panel (A), we present the thickness of Regions 1 and 3, as calculated from the density plots. As the solid-fluid attraction increases, these regions narrow and the methane density in Regions 1 and 3 increases, which is in qualitative agreement with the 2D density profiles presented in Figure 10. On the contrary, the methane density in Region 2 decreases, as confirmed by the density profiles shown in Figure 8. As a result, the diffusivity of methane in the 3 regions is expected to significantly change as the solid-fluid interactions increase. The number of molecules

in the 3 regions within these pores is summarized in Figure 9, panel (B). As the attraction between the surface and the fluid increases, the number of molecules adsorbed on the surface increases, leading to a reduced occupancy in the middle of the pore.

As the surface-methane attraction increases, the methane diffusion coefficient in Regions 1 and 3 was found to drop significantly, by almost one order of magnitude every time the solid-surface interaction was increased by 5 times, while the diffusivity in Region 2 increases moderately. However, we found the overall (total) diffusivity to remain constant. To explain these observations, our hypothesis is that the following two effects cancel each other out: 1) decreased R1 and R3 thickness, with correspondingly decreased diffusivity, and 2) increased R2 thickness, with correspondingly increased diffusivity.

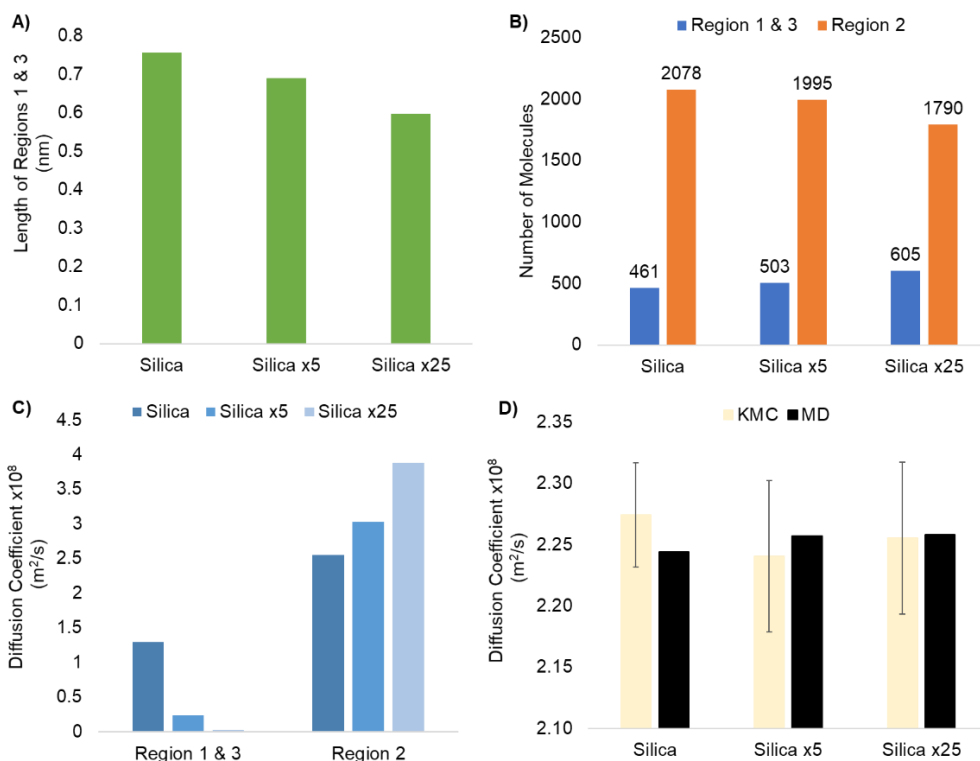


Figure 9. Analysis of the surface interaction effect on the width of Regions 1 & 3 (panel A), number of molecules absorbed (panel B), diffusivity in Regions 1,2, and 3 (panel C), and overall (total) diffusivity predicted using EMD simulations and the KMC model (panel D).

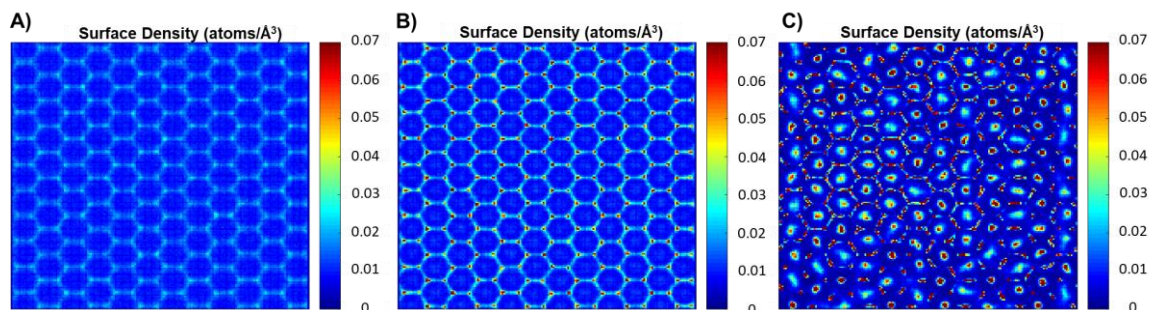


Figure 10. Surface density profiles for methane on the 3 silica-based systems as a function of surface-methane interactions. Panel (A) shows the realistic silica surface, while panels (B) and (C) the surfaces that are 5 and 25 times more attractive, respectively. Methane molecules in the first and second adsorbed layer were considered for this analysis.

3.3 3D KMC model validation

The 3D KMC model was validated against the analytical solution of the diffusion equation. To solve Eq. (8) and Eqs. (9-11), we considered a lattice containing 10 columns (X direction), 3 rows (Z direction), and 3 slices (Y direction). All boundaries were reflective: once a molecule reached a boundary, it bounced back to the lattice. 1350 molecules were distributed in the first third of the system, as shown in red in Figure 11, panel (A). The diffusion in all voxels within the lattice was set to $1 \times 10^{-8} \text{ m}^2/\text{s}$. We monitored the number of molecules in the 5th and 10th voxels over time, and solved Eqs. (8-11). The results obtained from the 3D KMC and those from the analytical equation are plotted in Figure 11 panels (B) and (C), respectively. Visual inspection confirms satisfactory agreement and shows that the stochastic results fluctuate around the deterministic ones. The fluctuations could be reduced by performing more independent runs and averaging the results.

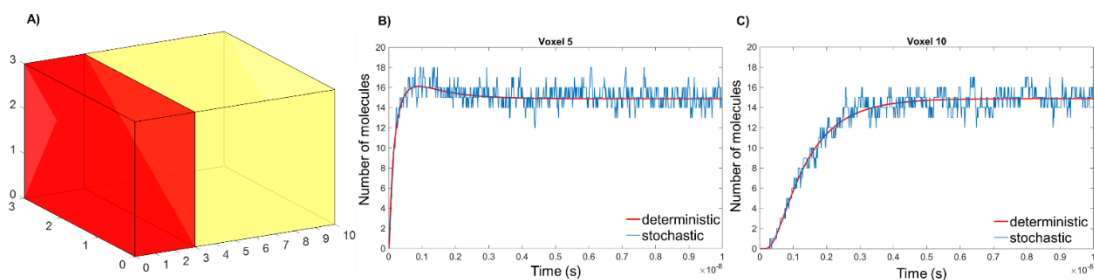


Figure 11. (A) Representation of the 3D KMC non-periodic system. The red region represents the area where the molecules were initially distributed. The comparison between the analytical equation and the 3D KMC predictions for (B) voxel 5 and (C) voxel 10, respectively.

The 3D KMC model was also tested for a homogeneous and periodic system. In this case, we set up 6 systems consisting of 5 columns (X direction), 6 rows (Z direction), and 3 slices (Y direction). We inserted 1 molecule and we allowed it to diffuse. We collected samples every 0.07 ns during a total of 70 ns of simulations. We then calculated the MSD from the trajectories, and the diffusion coefficient. Each system was homogeneous and the input (target) diffusion coefficient varied from 1.3×10^{-8} to $2.3 \times 10^{-8} \text{ m}^2/\text{s}$. In Figure 12 we present the MSDs calculated from the 6 systems (panel A) and the comparison between the input (target) and calculated diffusion coefficient (panel B) when using the 3D KMC algorithm.

We finally tested the effect of the unit cell size on the diffusion coefficient calculated by the 3D KMC approach. We found no statistically significant differences when using smaller or bigger unit cell sizes. This confirms the validity of the 3D KMC model in representing periodic systems. To test the 3D KMC model in a heterogeneous system we considered the 3 systems where the surface - fluid interaction was altered (see Section 3.2). We used the values reported in Figure 9 to set the diffusivity in Regions 1, 2, and 3. We used the algorithmic steps described in Figure 1, but for only 1 value of the pore width. From the trajectories obtained, we calculated the diffusion coefficient from 10 independent runs. The results are presented in Figure 9 panel (D), which shows agreement

between the KMC and EMD approaches, validating the applicability of the KMC model in heterogeneous systems.

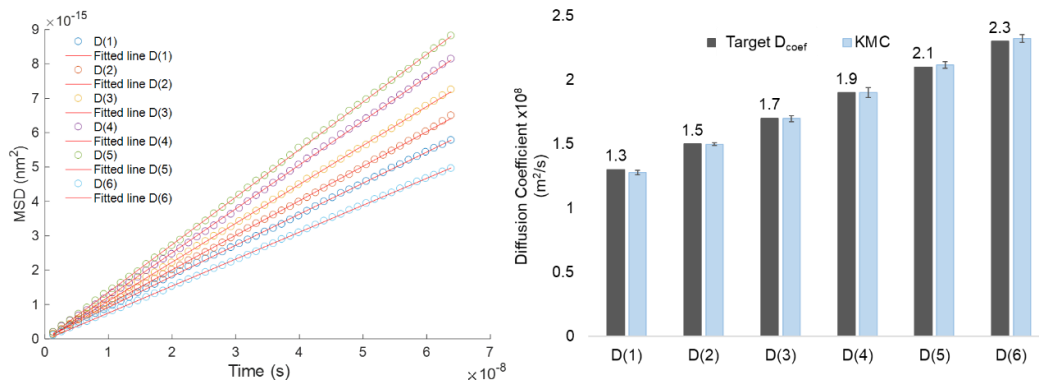


Figure 12. Validation of the 3D KMC algorithm using a periodic lattice.

3.4 3D KMC predictions of supercritical methane diffusivity in pores

In this Section we present the results obtained using the 3D KMC approach on the slit pore systems, using as input the results from atomistic EMD simulations. Regions 1, 2, and 3 were spatially defined within the KMC lattice based on density profiles such as those in Figure 4. The diffusion coefficients assigned to voxels within each region were the EMD results of Figure 5. To predict the overall (total) diffusivity in pores of increasing width, we followed the algorithm described in Figure 2. In Figure 13, we present the results obtained for the pores carved out of the 5 supports, for widths from 3 to 60 nm. Note that the limit of the X-axis in the five panels shown in Figure 13 changes from one system to another. This is because of the protocol we used to set up the 3D KMC systems, according to which the number of pore widths was the parameter used to determine the systems (35 pore widths for each substrate), together with the thickness of Regions 1 and 3, which differ among the substrates, as shown in Table 2. The KMC data are shown as blue

circles. The error bars calculated according to Eq. (12), considering 10 independent runs, are shown in red. The grey fitted line is a guide to the eye and the blue dashed line shows the diffusion coefficient of the bulk methane, as calculated from 3 independent EMD simulations in the bulk. It is helpful to remember that the density of the bulk methane is set to $0.01314 \text{ atoms}/\text{\AA}^3$ and the temperature is 300 K.

In all the pores considered, as the pore width increases, the diffusion coefficient of methane increases as well, until it reaches its bulk value, $1.91 \pm 0.08 \times 10^{-8} \text{ m}^2/\text{s}$. According to the results in Figure 13, the supercritical methane confined in MgO and silica slit-shaped pores exhibit bulk-like diffusivity when the pore width is slightly above 30 nm and 35 nm, respectively. Within the muscovite pores, supercritical methane reaches bulk behavior when the pore width is almost 40 nm. Within the alumina pores, this happens when the pore width is slightly wider than 37 nm, while in calcite the pore width required for supercritical methane to achieve bulk-like diffusivity is almost 50 nm. Our hypothesis is that this substrate-specific behavior is due to the preferential distribution of methane in Regions 1 and 3, near the solid substrates. While comparing the surface density profiles within the first adsorbed layer, presented in Figure 3, the MgO substrate shows the most uniform methane distribution, with silica, alumina, and muscovite substrates following. However, calcite exhibits sites that strongly attract methane. In a few pores, notably within silica, the results seem to suggest that in some cases the diffusion coefficient for the confined methane can be larger than that in the bulk. We ascribe this to numerical errors, which are quantified below, as we note that the datapoints correspondent to faster diffusion than bulk are consistent with bulk-like diffusion, when the error bars are considered.

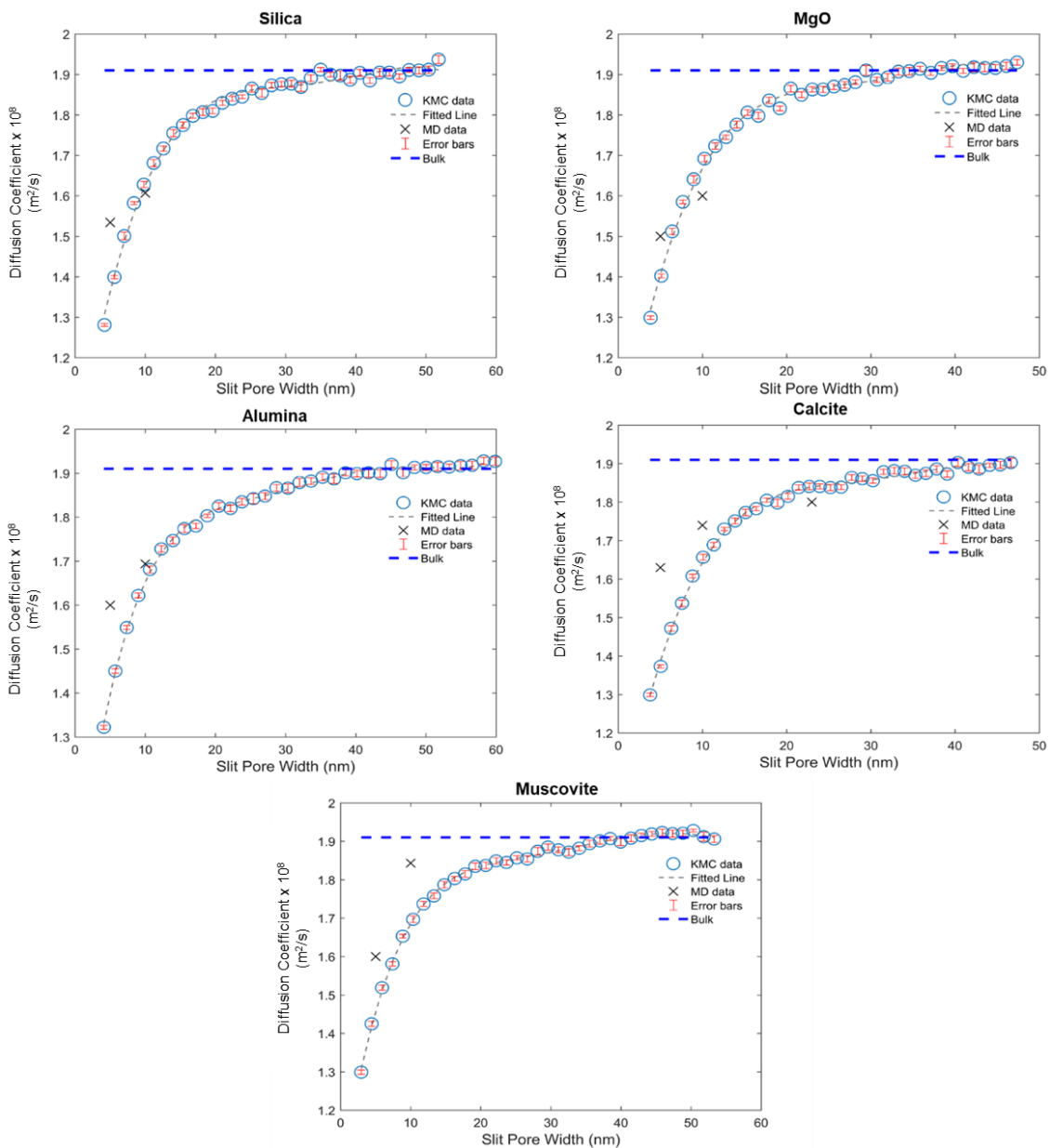


Figure 13. Overall (D_{xyz}) diffusion coefficient as a function of the pore width for the 5 solid supports considered here for the whole pore. Comparison between KMC predictions and EMD data. Note that the deviation between KMC and MD data is less than 10%.

In the five panels of Figure 13, we also report the diffusion coefficient data obtained by atomistic EMD simulations. For silica, MgO, alumina, and muscovite, there are 2 EMD data points, corresponding to 5 nm and 10 nm pore widths. For calcite, an additional data point is reported, at

25 nm width. The deviation between EMD data and KMC predictions in all cases is less than 10%. For the 5 nm pores, the % deviation is 8.8%, 8.1%, 7.4%, 9.3%, and 4.5% for silica, MgO, alumina, calcite, and muscovite pores, respectively, while for the 10 nm pores the % deviations become -1.3%, -4%, -0.8%, 6.1%, and 7.9%, respectively. From Figure 13 and the % deviations, it appears that the KMC predictions agree better with EMD data as the pore width increases. This is because of the diffusion coefficient assigned to Region 2. As discussed in Section 3.1, the diffusion coefficient in the pores center was very similar to the bulk value, albeit not identical; calcite exhibited a higher diffusion coefficient in Region 2, compared to the bulk, and the rest of the substrates slightly lower. It is expected that, as the pore width increases, the diffusion coefficient in Region 2 converges to the bulk, and the KMC input for the region becomes more accurate. This can be further confirmed by the 25 nm calcite pore, where the difference between the EMD and the KMC values is -2.3%.

Overall, the deviations between KMC and EMD data are satisfactorily small and presumably could be further reduced if more independent EMD simulations were performed and more accurate inputs were used to initiate the 3D KMC model, at the expense of increased demands on computational resources. Additional independent EMD simulations could also provide error bars and further aid the comparison between the two approaches. We note that in pores thinner than 5 nm, each parallel pore surface may interact with fluid molecules adsorbed near both walls, causing strong deviations from bulk-like behavior within the whole pore, even in its middle. In this case, the accuracy of the KMC model is expected to worsen and the % deviation between KMC and EMD simulations will potentially exceed the 10% threshold.

It should be emphasized that using the 3D KMC model for estimating self-diffusion coefficient in pores with varying pore width provides accurate results at very low computational cost. For the

5 nm pores considered, e.g., we performed atomistic EMD simulations for 53 ns for each solid. The time required for these calculations, using a supercomputer, ranged between 30 and 42 hours; the time required for conducting atomistic EMD simulations within the 10 nm and 25 nm simulations was higher, as the number of molecules increased. By comparison, the time required for the KMC simulations, per substrate, was approximately 35 minutes on the supercomputer to predict self-diffusion coefficient in pores of 35 different pore widths. The nodes used to perform these simulations consisted of 2 Intel Xeon E5-2683 v4 cores with 128 GB total RAM. For each pore width, 75 different initial configurations were tested in one simulation run, and 10 independent runs were performed, leading to a total of 26,250 simulations. This amount of simulations takes approximately 4 hours on a standard desktop computer, where it would be prohibitive for atomistic EMD simulations. Admittedly, transport models such as those discussed in Section 1, could be used to generate digital libraries similar to those shown in Figure 13. However, to make those models applicable for the systems investigated here, a certain number of parameters, usually obtained from EMD data, should be fitted to describe each substrate.⁷²

It should be noted that a numerical integrator of the Langevin's equation of motion could also be implemented, instead of the KMC approach proposed here, to describe the time evolution of a system.^{73,74} It has been reported that the selection of the integration step has pivotal impact on the accuracy of the results obtained by implementing the Langevin's approach, with shorter integration steps yielding more accurate results at the expense of higher computational cost. Similarly, several independent runs should be performed to ensure that accurate results are achieved when implementing the KMC protocol, which leads to increased computational cost. It is however expected that the KMC approach presented here could yield predictions for larger spatial scales and longer temporal scales than those achievable by solving Langevin's equation of motion,

because the stochastic KMC approach does not require resolving the diffusive trajectories of individual particles. For completeness, it should be noted that an innovative approach to numerically solve the master-equation (Eq. 6) was proposed by Kolokathis and Theodorou,⁷⁵ who simulated diffusion of xenon in silicalite-1. Their numerical approach was faster than KMC simulations, than solving numerically the master equation using the Euler method, and MD simulations by factors of $\sim 10^4$, 10^3 , and 10^7 , respectively. An alternative approach could also implement the work of Zaragoza et al.,⁷⁶ who proposed an equation that correlates diffusion coefficient and the viscosity. When considering wide pores, where the fluid viscosity is isotropic and homogeneous, this equation could produce results similar to those obtained from MD or the 3D KMC simulations discussed in this study.

4. CONCLUSIONS

We proposed and validated a methodology that synergistically implements atomistic equilibrium molecular dynamics (EMD) simulations and stochastic 3D kinetic Monte Carlo (KMC) calculations to predict self-diffusion coefficients for pure gases confined in pores as a function of pore width. In our analysis, we considered slit-shaped pores, but the methodology can be applied to cylindrical or rough pores as well. We started by performing atomistic EMD simulations in pores of moderate width (5 nm) and we used representative data, obtained within 3 regions within the pores, as input to construct a bespoke 3D KMC model that represents slit-shaped pores. We then implemented a sophisticated simulation protocol to obtain diffusion coefficients as a function of the pore width. The number of iterations and initializations implemented in this protocol ensured that the KMC data obtained for the various pore widths were statistically different.

Our proposed methodology acknowledges advantages and disadvantages of EMD and KMC approaches and implements each in the most efficient and impactful way. EMD simulations provided detailed and accurate atomic-scale data, which are necessary for obtaining accurate KMC calculations, at the expense of long run times. Because the computational time required by KMC is significantly shorter than that required by EMD, the KMC model was used to predict the methane diffusivity in pores of increasing pore width. Comparing KMC predictions to EMD simulations in pores of width 10 and 25 nm, we found that the % deviation between the two methods is less than 10% for all cases considered here. The combined EMD-KMC approach allowed us to obtain a digital library that matches diffusivity to pore widths and pore chemistry at minimum computational cost. Within the pores considered, it was found that confinement reduces the methane diffusivity, and that bulk-like diffusivity is reached when the pore width is at least 30 nm, and in some cases more than 50 nm, depending on pore chemistry. This digital library can be used, in the future, to simulate realistic 3D pore networks.

The methodology proposed is expected to be applicable to study gasses at different densities and temperatures, as well as mixtures. While the approach is expected to be useful for predicting gas permeability in shale samples, many applications that involve fluid transport across pore networks, including catalysis, could benefit from the methodology presented here.

ASSOCIATED CONTENT

Supporting Information

The Supporting Information is available free of charge on the ACS Publications website at DOI: (to be filled).

RDF profiles for the 5 nm wide pores (PDF).

AUTHOR INFORMATION

Corresponding Author

*Email: a.striolo@ucl.ac.uk

Funding Sources

We would like to thank financial support provided by Halliburton and the European Union's Horizon 2020 research and innovation program under Grant Agreement No. 764810.

Notes

The authors declare no competing financial interest

ACKNOWLEDGEMENT

The authors would like to thank Professor John M. Shaw of the Chemical and Materials Engineering Department at University of Alberta for his critical comments and recommendations. Prof. Shaw's sabbatical at UCL was supported, in part, by grant number VP2-2017-023 from the Leverhulme Trust. The authors acknowledge the use of the UCL Legion High Performance Computing Facility (Legion@UCL), and associated support services, in the completion of this work. MA was sponsored by a studentship provided, in part, by Halliburton, which is kindly acknowledged.

REFERENCES

1. Energy Information Administration (EIA). Shale Gas Production. *Nat Gas*. 2014:123-152.
2. BP. *Energy Outlook*.; 2019.
3. Boyer C, Clark B, Jochen V, Lewis R, Dallas CKM. *Shale Gas: A Global Resource*. Vol 23.; 2011.
4. Montgomery SL, Jarvie DM, Bowker KA, Pollastro RM. Mississippian Barnett Shale, Fort Worth basin, north-central Texas: Gas-shale play with multi-trillion cubic foot potential. *Am Assoc Pet Geol Bull*. 2005;89(2):155-175.
5. Loucks RG, Reed RM, Ruppel SC, Jarvie DM. Morphology, Genesis, and Distribution of Nanometer-Scale Pores in Siliceous Mudstones of the Mississippian Barnett Shale. *J Sediment Res*. 2009;79(12):848-861.
6. Sondergeld CH, Ambrose RJ, Rai CS, Moncrieff J. Micro-structural studies of gas shales. *SPE Unconv Gas Conf 23-25 February, Pittsburgh, Pennsylvania, USA SPE 131771-MS*. 2010.
7. Backeberg NR, Iacoviello F, Rittner M, et al. Quantifying the anisotropy and tortuosity of permeable pathways in clay-rich mudstones using models based on X-ray tomography. *Sci Rep*. 2017;7(1):1-12.
8. Boyer C, Kieschnick J, Suarez-Rivera R, Lewis RE, Waters G. *Producing Gas from Its Source*. Vol 18.; 2006.
9. Sondergeld CH, Newsham KE, Comisky JT, Rice MC, Rai CS. Petrophysical Considerations in Evaluating and Producing Shale Gas Resources. *SPE Unconv Gas Conf held Pittsburgh, Pennsylvania, USA, 23–25 Febr 2010 SPE 131768-MS*. 2010.

10. Josh M, Esteban L, Delle Piane C, Sarout J, Dewhurst DN, Clennell MB. Laboratory characterisation of shale properties. *J Pet Sci Eng*. 2012;88-89:107-124.
11. Heller R, Zoback M. Adsorption of methane and carbon dioxide on gas shale and pure mineral samples. *J Unconv Oil Gas Resour*. 2014;8(C):14-24.
12. Ross DJK, Marc Bustin R. The importance of shale composition and pore structure upon gas storage potential of shale gas reservoirs. *Mar Pet Geol*. 2009;26(6):916-927.
13. Ma L, Fauchille A-L, Doweij PJ, et al. Correlative multi-scale imaging of shales: a review and future perspectives. *Geol Soc London, Spec Publ*. 2017;454(1):175-199.
14. Li J, Sultan AS. Permeability Computations of Shale Gas by the Pore-scale Monte Carlo Molecular Simulations. *Int Pet Technol Conf held Doha, Qatar, 6-9 December 2015 IPTC-18263-MS*. 2015:1-10.
15. Chen C, Hu D, Westacott D, Loveless D. Nanometer-scale characterization of microscopic pores in shale kerogen by image analysis and pore-scale modeling. *Geochemistry, Geophys Geosystems*. 2013;14(10):4066-4075.
16. Tahmasebi P, Javadpour F, Sahimi M. Stochastic shale permeability matching: Three-dimensional characterization and modeling. *Int J Coal Geol*. 2016;165:231-242.
17. He S, Jiang Y, Conrad JC, Qin G. Molecular simulation of natural gas transport and storage in shale rocks with heterogeneous nano-pore structures. *J Pet Sci Eng*. 2015;133:401-409.
18. Cole DR, Striolo A. The Influence of Nanoporosity on Carbon-Bearing Fluids. In: *Deep Carbon: Past to Present*. New York, USA: Cambridge University Press; 2019.

19. Sui H, Yao J, Zhang L. Molecular Simulation of Shale Gas Adsorption and Diffusion in Clay Nanopores. *Computation*. 2015;3(4):687-700.
20. Vasileiadis M, Peristeras LD, Papavasileiou KD, Economou IG. Transport Properties of Shale Gas in Relation to Kerogen Porosity. *J Phys Chem C*. 2018;122(11):6166-6177.
21. Wang S, Feng Q, Zha M, Javadpour F, Hu Q. Supercritical Methane Diffusion in Shale Nanopores: Effects of Pressure, Mineral Types, and Moisture Content. *Energy and Fuels*. 2018;32(1):169-180.
22. Phan A, Cole DR, Wei RG, Dzubiella J, Striolo A. Confined Water Determines Transport Properties of Guest Molecules in Narrow Pores. *ACS Nano*. 2016;10(8):7646-7656.
23. Bui T, Phan A, Cole DR, Striolo A. Transport Mechanism of Guest Methane in Water-Filled Nanopores. *J Phys Chem C*. 2017;121(29):15675-15686.
24. Berendsen HJC. *Computational Molecular Dynamics: Challenges, Methods, Ideas*.; 1999.
25. Phan A, Striolo A. Microporous and Mesoporous Materials Methane transport through hierarchical silica micro-mesoporous materials: From non-equilibrium atomistic simulations to phenomenological correlations. *Microporous Mesoporous Mater*. 2019;288:109559.
26. Akkutlu IY, Fathi E. Multiscale Gas Transport in Shales With Local Kerogen Heterogeneities. *SPE Annu Tech Conf Exhib Denver, 30 October–2 November SPE - 146422-MS*. 2012.
27. Krishna R, Wesselingh JA. Review Article Number 50-The Maxwell-Stefan approach to mass transfer. *Science (80-)*. 1997;52(6):861-911.

28. Javadpour F. Nanopores and apparent permeability of gas flow in mudrocks (shales and siltstone). *J Can Pet Technol*. 2009;48(8):16-21.
29. Wu K, Chen Z, Li X, Guo C, Wei M. A model for multiple transport mechanisms through nanopores of shale gas reservoirs with real gas effect-adsorption-mechanic coupling. *Int J Heat Mass Transf*. 2016;93:408-426.
30. Wu K, Li X, Wang C, Chen Z, Yu W. A Model for Gas Transport in Microfractures of Shale and Tight Gas Reservoirs. *AIChE J*. 2015;61(6):2079-2087.
31. Apostolopoulou M, Dusterhoft R, Day R, Stamatakis M, Coppens MO, Striolo A. Estimating permeability in shales and other heterogeneous porous media: Deterministic vs. stochastic investigations. *Int J Coal Geol*. 2019;205:140-154.
32. Kratzer P. Monte Carlo and kinetic Monte Carlo methods. *Multiscale Simul Methods Mol Sci*. 2009;42:51-76.
33. Darby MT, Piccinin S, Stamatakis M. First principles-based kinetic Monte Carlo simulation in catalysis. In: *Physics of Surface , Interface and Cluster Catalysis*. 2nd ed. Bristol, UK: IOP Publishing, Bristol, UK; 2016:1-38.
34. Apostolopoulou M, Day R, Hull R, Stamatakis M, Striolo A. A kinetic Monte Carlo approach to study fluid transport in pore networks. *J Chem Phys*. 2017;147(134703):1-10.
35. Naraghi ME, Javadpour F. A stochastic permeability model for the shale-gas systems. *Int J Coal Geol*. 2015;140:111-124.
36. Phan A, Cole DR, Striolo A. Preferential Adsorption from Liquid Water-Ethanol Mixtures in Alumina Pores. *Langmuir*. 2014;30:8066-8077.

37. Phan A, Cole DR, Striolo A. Aqueous Methane in Slit-Shaped Silica Nanopores: High Solubility and Traces of Hydrates. *J Phys Chem C*. 2014;118:4860-4868.
38. Argyris D, Ho T, Cole DR, Striolo A. Molecular Dynamics Studies of Interfacial Water at the Alumina Surface. *J Phys Chem C*. 2011;115:2038-2046.
39. Argyris D, Tummala NR, Striolo A. Molecular Structure and Dynamics in Thin Water Films at the Silica and Graphite Surfaces. *J Phys Chem C*. 2008;112:13587-13599.
40. Ho TA, Striolo A. Water and Methane in Shale Rocks: Flow Pattern Effects on Fluid Transport and Pore Structure. *AIChE J*. 2015;61(9):2993-2999.
41. Ho TA, Argyris D, Papavassiliou D V., Striolo A, Lee LL, Cole DR. Interfacial water on crystalline silica: a comparative molecular dynamics simulation study. *Mol Simul*. 2011;37(3):172-195.
42. Causa M, Dovesi R, Pisani C, Roetti C. Ab initio Hartree-Fock study of the MgO(001) surface. *Surf Sci*. 1986;175:551-560.
43. Scamehorn C, Hess A, McCarthy M. Correlation corrected periodic Hartree-Fock study of the interactions between water and the (001) magnesium oxide surface. *J Chem Phys*. 1993;99:2786-2795.
44. Cygan RT, Liang J-J, Kalinichev AG. Molecular Models of Hydroxide, Oxyhydroxide, and Clay Phases and the Development of a General Force Field. *J Phys Chem B*. 2004;108(4):1255-1266.
45. Xiao S, Edwards SA, Gräter F. A new transferable forcefield for simulating the mechanics of CaCO₃ crystals. *J Phys Chem C*. 2011;115(41):20067-20075.

46. Martin MG, Siepmann JI. Transferable Potentials for Phase Equilibria. 1. United-Atom Description of n -Alkanes. *J Phys Chem B*. 1998;102(97):2569-2577.
47. Jorgensen WL, Maxwell DS, Tirado-Rives J. Development and testing of the OPLS all-atom force field on conformational energetics and properties of organic liquids. *J Am Chem Soc*. 1996;118(45):11225-11236.
48. Ho TA, Criscenti LJ, Wang Y. Nanostructural control of methane release in kerogen and its implications to wellbore production decline. *Sci Rep*. 2016;6(28053):1-9.
49. Feng H, Gao W, Nie J, et al. MD simulation of self-diffusion and structure in some n-alkanes over a wide temperature range at high pressures. *J Mol Model*. 2013;19(1):73-82.
50. Essmann U, Perera L, Berkowitz ML, Darden T, Lee H, Pedersen LG. A smooth particle mesh Ewald method. *J Chem Phys*. 1995;103(19):8577-8593.
51. Lorentz HA. Ueber die Anwendung des Satzes vom Virial in der kinetischen Theorie der Gase. *Ann Phys*. 1881;248(1):127-136.
52. Berthelot D. Sur Le Mélange Des Gaz. *Compt Rendus*. 1898;126:1703-1706.
53. Siperstein F, Myers AL, Talu O. Long range corrections for computer simulations of adsorption. *Mol Phys*. 2002;100(13):2025-2030.
54. Tian Y, Yan C, Jin Z. Characterization of Methane Excess and Absolute Adsorption in Various Clay Nanopores from Molecular Simulation. *Sci Rep*. 2017;7(12040):1-21.
55. Kowalczyk P, Tanaka H, Kaneko K, Terzyk AP, Do DD. Grand canonical Monte Carlo simulation study of methane adsorption at an open graphite surface and in slitlike carbon

- pores at 273 K. *Langmuir*. 2005;21(12):5639-5646.
56. Van Der Spoel D, Lindahl E, Hess B, Groenhof G, Mark AE, Berendsen HJC. GROMACS: Fast, flexible, and free. *J Comput Chem*. 2005;26(16):1701-1718.
 57. Hess B, Kutzner C, Van Der Spoel D, Lindahl E. GROMACS 4: Algorithms for highly efficient, load-balanced, and scalable molecular simulation. *J Chem Theory Comput*. 2008;4(3):435-447.
 58. Nosé S. A molecular dynamics method for simulations in the canonical ensemble A molecular dynamics method for simulations in the canonical ensemble. *Mol Phys*. 1984;52(2):255-268.
 59. Hoover WG. Canonical dynamics: Equilibrium phas-space distributions. *Phys Rev A*. 1985;31(3):1695-1697.
 60. Hockney RW, Goel SP, Eastwood JW. Quiet High-Resolution Computer Models of a Plasma. *J Comput Phys*. 1974;14(2):148-158.
 61. Simonnin P, Noetinger B, Nieto-Draghi C, Marry V, Rotenberg B. Diffusion under Confinement: Hydrodynamic Finite-Size Effects in Simulation. *J Chem Theory Comput*. 2017;13(6):2881-2889.
 62. Yeh I, Hummer G. System-Size Dependence of Diffusion Coefficients and Viscosities from Molecular Dynamics Simulations with Periodic Boundary Conditions. *J Phys Chem B*. 2004;108(40):15873-15879.
 63. Le TTB, Striolo A, Cole DR. Structural and dynamical properties predicted by reactive force fields simulations for four common pure fluids at liquid and gaseous non-reactive

- conditions. *Mol Simul.* 2018;44(10):826-839.
64. Moulτος OA, Zhang Y, Tsimpanogiannis IN, Economou IG, Maginn EJ. System-size corrections for self-diffusion coefficients calculated from molecular dynamics simulations: The case of CO₂, n -alkanes, and poly(ethylene glycol) dimethyl ethers. *J Chem Phys.* 2016;145(074109):1-6.
 65. Jamali SH, Wolff L, Becker TM, Bardow A, Vlugt TJH, Moulτος OA. Finite-Size Effects of Binary Mutual Diffusion Coefficients from Molecular Dynamics. *J Chem Theory Comput.* 2018;14(5):2667-2677.
 66. Van Kampen N. The Master Equation. In: *Stochastic Processes in Physics and Chemistry.* ; 2007:96-133.
 67. Matsumoto M, Nishimura T. Dynamic creation of pseudorandom number generators. *Monte Carlo and Quasi-Monte Carlo Methods.* 2000;1(1):56-69.
 68. Crank J. Methods of solution when the diffusion coefficient is constant. In: *The Mathematics of Diffusion.* 2nd ed. Oxford, UK: Oxford University Press; 1975:11-27.
 69. Jansen APJ. *An Introduction to Kinetic Monte Carlo Simulations of Surface Reactions.* Berlin, Germany: Springer-Verlag Berlin Heidelberg; 2012.
 70. Flamm MH, Diamond SL, Sinno T. Lattice kinetic Monte Carlo simulations of convective-diffusive systems. *J Chem Phys.* 2009;130(9).
 71. Franco LFM, Castier M, Economou IG. Anisotropic parallel self-diffusion coefficients near the calcite surface: A molecular dynamics study. *J Chem Phys.* 2016;145(8).

72. Kou R, Alafnan SFK, Akkutlu IY, Texas A, Station C. Coupling of Darcy ' s Equation with Molecular Transport and its Application to Upscaling Kerogen Permeability. *SPE Eur Featur 78th EAGE Conf Exhib 30 May-2 June, Vienna, Austria SPE-180112-MS*. 2016:1-16.
73. Comer J, Aksimentiev A. Predicting the DNA Sequence Dependence of Nanopore Ion Current Using Atomic-Resolution Brownian Dynamics. *J Phys Chem C*. 2012;(116):3376–3393.
74. Vardavas R. Fluctuations and scaling in 1D irreversible film growth models . 2002.
75. Kolokathis PD, Theodorou DN. On solving the master equation in spatially periodic systems On solving the master equation in spatially periodic systems. *J Chem Phys*. 2012;137(034112):1-21.
76. Zaragoza A, Gonzalez MA, Joly L, et al. Molecular dynamics study of nanoconfined TIP4P/2005 water: How confinement and temperature affect diffusion and viscosity. *Phys Chem Chem Phys*. 2019;21(25):13653-13667.